Aalto University

OPEN ACCESS

This is an electronic reprint of the original article.
This reprint may differ from the original in pagination and typographic detail.

Jana, Arijit; Dar, Wakeel Ahmed; Jana, Sourav Kanti; Poonia, Ajay Kumar; Yadav, Vivek; Roy, Jayoti; Chandra, Sourov; Adarsh, Kumaran Nair Valsala Devi; Ras, Robin H. A.; Pradeep, Thalappil

Photoconversion of Ag31 to Ag42 Initiated by Solvated Electrons

Published in:
Chemistry of Materials

DOI:
10.1021/acs.chemmater.3c01293

Published: 12/09/2023

Document Version
Publisher's PDF, also known as Version of record

Published under the following license:
CC BY

Please cite the original version:
Jana, A., Dar, W. A., Jana, S. K., Poonia, A. K., Yadav, V., Roy, J., Chandra, S., Adarsh, K. N. V. D., Ras, R. H. A., & Pradeep, T. (2023). Photoconversion of Ag31 to Ag42 Initiated by Solvated Electrons. *Chemistry of Materials*, *35*(17), 7020–7031. https://doi.org/10.1021/acs.chemmater.3c01293

This material is protected by copyright and other intellectual property rights, and duplication or sale of all or part of any of the repository collections is not permitted, except that material may be duplicated by you for your research use or educational purposes in electronic or print form. You must obtain permission for any other use. Electronic or print copies may not be offered, whether for sale or otherwise to anyone who is not an authorised user.

CHEMISTRY OF MATERIALS

pubs.acs.org/cm

Article

Open Access

This article is licensed under CC-BY 4.0

Photoconversion of Ag_{31} to Ag_{42} Initiated by Solvated Electrons

Arijit Jana, Wakeel Ahmed Dar, Sourav Kanti Jana, Ajay Kumar Poonia, Vivek Yadav, Jayoti Roy, Sourov Chandra, Kumaran Nair Valsala Devi Adarsh,* Robin H. A. Ras,* and Thalappil Pradeep*

Cite This: *Chem. Mater.* 2023, 35, 7020−7031

Read Online

ACCESS | Metrics & More | Article Recommendations | Supporting Information

ABSTRACT: Light-matter interactions, especially in atomically precise nanomaterials, belong to an unexplored realm of research with potential benefits for the synthesis of materials. Here, we present an interesting light-activated expansion process of an Ag_{31} nanocluster to an Ag_{42} analogue, both clusters being protected with 6-(dibutylamino)-1,3,5-triazine-2, 4-dithiol (shortly, TRZ-H_2) ligands. The conversion process was initially monitored through UV−vis, revealing that the violet-colored Ag_{31} got converted to greenish Ag_{42}, exhibiting their characteristic absorption features. High-resolution mass spectrometric studies confirmed that the as-synthesized $[Ag_{31}(TRZ)_{10}]$ with coexisting di- and monoanionic charged species in dichloromethane solution got converted to $[Ag_{42}(TRZ)_{13}]$ with a dipositive charge state. Electrochemical studies revealed the photoresponsive nature of Ag_{31}, and light illumination resulted in transient intermediate clusters covered with solvated electrons, which contributed to the core expansion. Ag_{31} is NIR-emitting, while Ag_{42} is red-emitting. The ultrafast transient absorption studies reveal that Ag_{42} has strikingly short excited-state carrier dynamics than Ag_{31}. The stable excited-state carriers for Ag_{31} upon photoexcitation also underline the unique electronic characteristics responsible for such light-activated structural evolution.

Downloaded via AALTO UNIV on October 6, 2023 at 06:27:03 (UTC).
See https://pubs.acs.org/sharingguidelines for options on how to legitimately share published articles.

INTRODUCTION

Atomically precise metal nanoclusters (NCs) with a kernel of metal atoms, protected by various ligands, connecting the gap between traditional nanoparticles and single atoms, have emerged as a new class of functional nanomaterials with unique optical and physicochemical properties.[1−6] Such type of ultrasmall nanoparticles with a core dimension <3 nm displayed exotic optical properties, such as molecule-like multiple absorption and emission due to the electronic transitions between their discrete energy levels.[7−9] A wide range of silver NCs with varying nuclearities, such as Ag_6, Ag_{14}, Ag_{16}, Ag_{21}, Ag_{25}, Ag_{29}, Ag_{35}, Ag_{40}−Ag_{46}, Ag_{61}, Ag_{67}, Ag_{146}, Ag_{374}, and so forth, with protecting ligands were synthesized, and some of them have been structurally characterized using single-crystal X-ray diffraction studies.[1−3,10−21] Atomic arrangements of such nanomaterials, associated energy levels, and surface reactivity promote their potential applications in the fields of catalysis, molecular recognition, biomedical imaging, and optoelectronic devices.[22−29] The stability of silver NCs mainly depends on the outer coverage of surface ligands. The bare NCs without ligands are highly reactive, and they react to themselves or with species in the surrounding environments and form larger particles or adduct species.[30] Different surface ligands, such as thiol, imine thiol, selenol, phosphine, carboxylic acid, calixarene, alkynyl, and so forth, create clusters with higher stability than bare NCs.[31−40] Generally, thiolated silver NCs are more stable than phosphine, hydride, and alkyne-protected ones.[1−3] We have introduced a new bidentate thiol ligand for silver clusters, i.e., 6-(dibutylamino)-1, 3, 5-triazine-2, 4-dithiol (shortly, TRZ-H_2) having two butyl chains connected through a nitrogen atom and a triazine ring. Steric bulk created by two butyl chains attached to the triazine ring makes this ligand more attractive than their bidentate thiol analogues such as benzene-dithiol.[15] The electron-withdrawing ability of three nitrogens present in the triazine ring makes it less electron-dense than benzene. The enhanced polarizability of the heterocycle rather than benzene makes the $\pi-\pi^*$ electronic transition of the triazine ligand different from the benzene analogues.[41,42] Recently, we have demonstrated the multifunctional optoelectronic and quantum coherence behavior of an ultrasmall Au_6 NC protected by the same ligand.[43]

The past decade has witnessed the synthesis of various silver NCs and an understanding of their structure−property correlations. These nanomaterials spontaneously change their nuclearity, size, and shape upon change in parameters such as temperature, pressure, solvents, external metal ions, and so

Received: May 26, 2023
Revised: August 15, 2023
Published: August 31, 2023

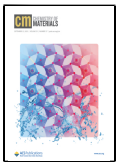

© 2023 American Chemical Society

https://doi.org/10.1021/acs.chemmater.3c01293
Chem. Mater. 2023, 35, 7020−7031

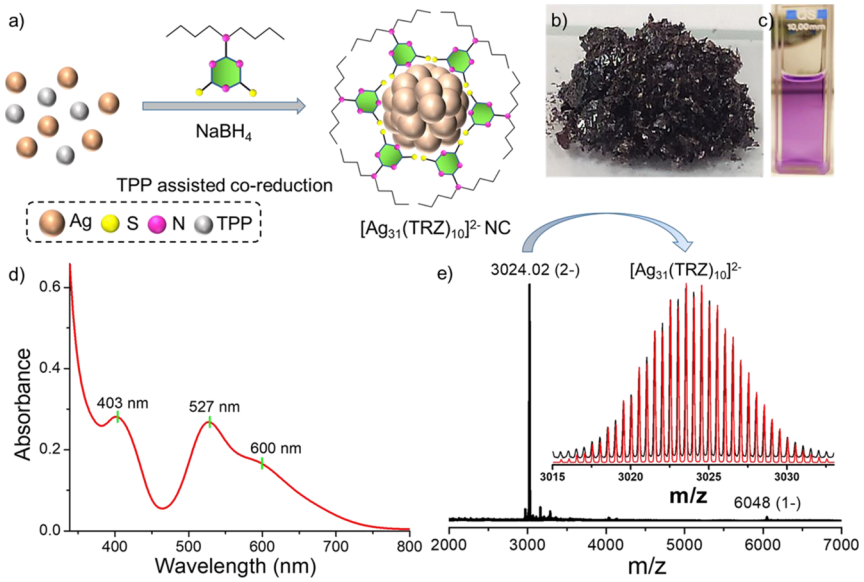

Figure 1. (a) Schematic representation of the synthesis of Ag_{31} using the triphenylphosphine-assisted coreduction reaction. Photographs of (b) 200 mg powder of Ag_{31} and (c) violet-colored Ag_{31} in DCM. (d) UV−vis absorption spectrum of the cluster. (e) Full range ESI-MS spectrum in the negative-ion mode. An intense dianionic peak at m/z 3024.02 and a monoanionic peak at 6048.01 indicate the presence of both the charge states of the cluster. The inset shows the isotopic distribution of the experimental (black) and theoretical (red) spectra.

forth.[44−48] For example, enhanced emission at a low temperature was observed for silver NCs due to the modulation of their optical band gap.[49,50] Zang and co-workers observed a visible color change in a single crystal of silver-sulfide NC due to its structural strain at high pressure.[51] Along with a visible color change, bathochromic shifting of the emission maxima with luminescence enhancement was also observed for different silver NCs.[52,53] Interconversion of silver NCs promoted by solvents and counterions is also manifested in their surface sensitivity.[54,55] Recently, we have illustrated metal−metal and metal−sulfide structural rearrangements of silver NCs promoted by external bidentate organic linkers resulting in functional metal−organic framework solids.[56] Compared to other stimuli, the effect of light exposure to silver NCs is not well explored. However, silver nanoparticles and nanostructures are known for their light sensitivity.[57−59] Photoinduced structural effects of various silver nanostructures lead to their applications in plasmon-assisted polymerization, photodriven chemical transformations, photochromic effects, surface-enhanced Raman scattering, and so forth.[60−64] Interactions between electromagnetic radiation and surface-bound free electrons are responsible for such type of photochemical effects. In this context, a detailed understanding of the interaction between newly synthesized silver NCs and light is an actively pursued research frontier.

In the present work, we present the synthesis of a TRZ-H_2 protected silver NC, i.e., $[Ag_{31}(TRZ)_{10}]$ (shortly Ag_{31}) using triphenylphosphine-assisted metal thiolate coreduction reaction. This is the first report of a silver NC protected by triazine dithiol ligand. Due to the specific metal core and surface ligand arrangements, it shows a characteristic UV−visible absorption feature having three absorption maxima at 403, 527, and 600 nm. High-resolution mass spectrometry (MS) and other spectroscopic and microscopic studies confirm the atomic arrangement of the cluster. Thermogravimetric analysis shows the thermal stability of the cluster in the solid state, and time-dependent UV−vis shows the stability of the cluster in solution. Interestingly, we have observed that the violet-colored Ag_{31} got converted to greenish Ag_{42} upon white light illumination. MS investigations reveal the formation of a new cluster, i.e., $[Ag_{42}(TRZ)_{13}]$, with higher nuclearity. The photoluminescence (PL) studies show that NIR-emitting Ag_{31} got converted to red-emitting Ag_{42}. The formation of mixed intermediate clusters with photogenerated electrons by light exposure is probably the reason behind such a structural expansion. Ultrafast transient absorption studies further reveal the unique characteristics of the excited-state carriers in these clusters. This work demonstrates the potential of light-activated conversion of ligand-protected NCs with specific optical and photophysical characteristics. Although there is a large body of data on these clusters, their single crystals were not obtained to determine their structures.

EXPERIMENTAL SECTION

Chemicals. Silver nitrate ($AgNO_3$) was purchased from Rankem Chemicals. Sodium borohydride ($NaBH_4$, 98%) and triphenylphosphine (TPP) were bought from Aldrich Chemicals. The ligand, TRZ-H_2, was purchased from TCI America. Sodium sulfate and tetrabutylammonium hexafluorophosphate (TBAF) were purchased from Fisher Scientific and Aldrich, respectively. Solvent grade dichloromethane (DCM), chloroform ($CHCl_3$), *n*-hexane, *N*,*N*-dimethylformamide, and methanol were bought from Rankem chemicals and Finar, India. Milli-Q water was used for the synthesis and purification of clusters. Deuterated solvent, $CDCl_3$ (99.8 atom % D), was purchased from Sigma Aldrich. All chemicals are commercially available and were used as such without further purification.

Synthesis of Ag_{31} NC. Ag_{31} was synthesized at room temperature using a triphenylphosphine-assisted silver-thiolate coreduction reaction. In brief, 20 mg of $AgNO_3$ (0.12 mM) was dissolved in 5 mL of methanol. 25 mg of TRZ-H_2 (0.09 mM) was dissolved in 9 mL of DCM and added to the stirring condition. After 15 min of reaction, 75 mg of TPP (0.28 mM) dissolved in 2 mL of DCM was added to the reaction mixture. After 10 min of reaction, 12−13 mg of $NaBH_4$ dissolved in 1 mL of Milli-Q water was added. After adding $NaBH_4$, a dark reddish solution was formed, which eventually was converted to a bluish-violet solution after an overnight reaction. After 12 h of reaction, mixed solvents were removed at reduced pressure. The crude

https://doi.org/10.1021/acs.chemmater.3c01293
Chem. Mater. 2023, 35, 7020−7031

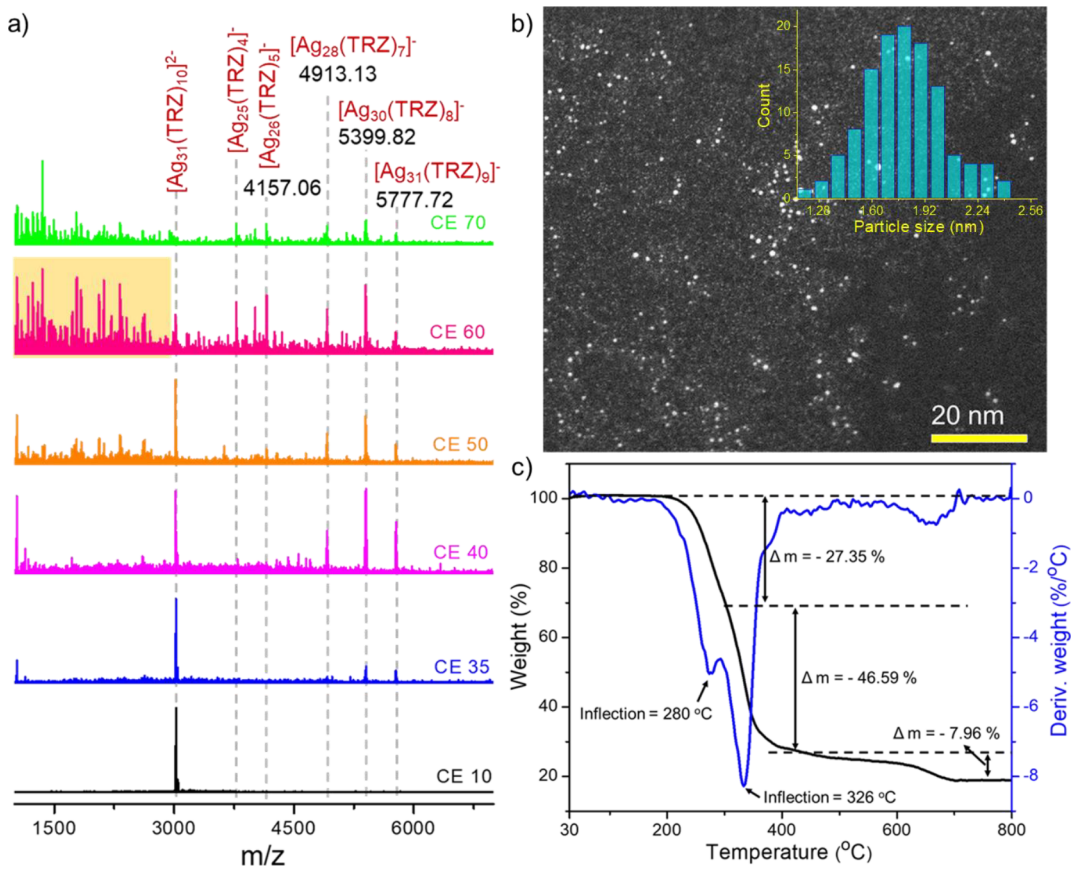

Figure 2. (a) Collision energy-dependent MS/MS fragmentation spectra of Ag_{31} shows the losses of TRZ and silver fragments from the parent cluster. An expanded view of the highlighted region is shown in the Supporting Information. (b) Scanning transmission electron microscopic image of the Ag_{31} NC. The inset shows the particle size distribution profile with an average diameter of 1.8 ± 0.21 nm. (c) Thermogravimetric analysis and differential thermal analysis of Ag_{31} indicating its thermal stability up to 280 °C.

oily product was cleaned five to six times using methanol and hexane in ultrasonic condition to make pure dark violet-colored powder. The yield of the product was 75% in terms of silver.

Light-Triggered Conversion. The Ag_{31} powder (3 mg) was dissolved in 3 mL of DCM or chloroform in a clean glass bottle to study the light-illuminated conversion process. A white light source (xenon arc lamp with a power of 100−200 W) from Newport, India was used for irradiation. Continuous exposure to light leads to such intercluster conversion, which was initially monitored by the visible change in the color of the solution. To further verify the conversion, UV−vis absorption and MS studies were performed. The yield of the interconverted Ag_{42} cluster is 30−35% in terms of the Ag_{31} cluster.

RESULTS AND DISCUSSION

Synthesis and Characterization of Ag_{31}. We have synthesized TRZ-protected Ag_{31} at room temperature (25 °C) by triphenylphosphine-assisted coreduction of silver thiolate precursor using $NaBH_4$ as the reducing agent. Figure 1a shows the schematic representation of the synthesis. A detailed synthesis protocol of Ag_{31} is presented in the Experimental Section. The formation of Ag_{31} was monitored using time-dependent UV−vis (Figure S1), which shows the appearance of characteristic absorption bands after 6 h of reaction and which eventually becomes more prominent after the overnight reaction. The purified cluster was used for further studies. Photographs in Figure 1b,c depict the violet-colored cluster in the solid state and in DCM solution, respectively. UV−vis absorption characterized the Ag_{31}, representing discrete spectral bands at 403, 527, and 600 nm (Figure 1d). The characteristic spectral feature is the fingerprint of the NC. To understand the effect of TPP in the synthesis, we performed a reaction with equal amounts of metal and thiolate precursors without TPP. The product formed due to the reduction without TPP is red, unlike violet-colored Ag_{31} with TPP. UV−vis absorption spectrum is also not similar in both the cases (shown in Figure S2). Furthermore, we successfully scaled up the synthesis (5-fold) of Ag_{31} through TPP-assisted reduction reaction, which was verified through UV−vis studies (Figure S3).

The molecular composition of the Ag_{31} was substantiated using high-resolution electrospray ionization mass spectrometry (HR-ESI-MS) studies. Additional details of instrumentation and sample preparation are presented in the Supporting Information. Figure 1e shows the negative-ion mode ESI-MS spectrum of the cluster with an intense ion peak at m/z 3024.02 and a relatively weak peak at m/z 6048.01. A peak-to-peak separation of isotopic distribution is 0.5 for m/z 3024.02 and 1 for m/z 6048.01 peaks, confirming that the charge states of the ions were 2 and 1, respectively. The total mass of 6048.01 matches with the composition of $[Ag_{31}(TRZ)_{10}]$, coexisting with the di- and monoanionic charge state species. The isotopic envelope matches well with the theoretical spectrum (shown in the inset of Figure 1e). We did not observe any peak in the spectrum collected in the positive-ion mode (Figure S4), manifesting the lack of additional cationic species. Upon additional MS measurements using cesium acetate as the ionizing agent, we observed the emergence of

https://doi.org/10.1021/acs.chemmater.3c01293
Chem. Mater. 2023, 35, 7020−7031

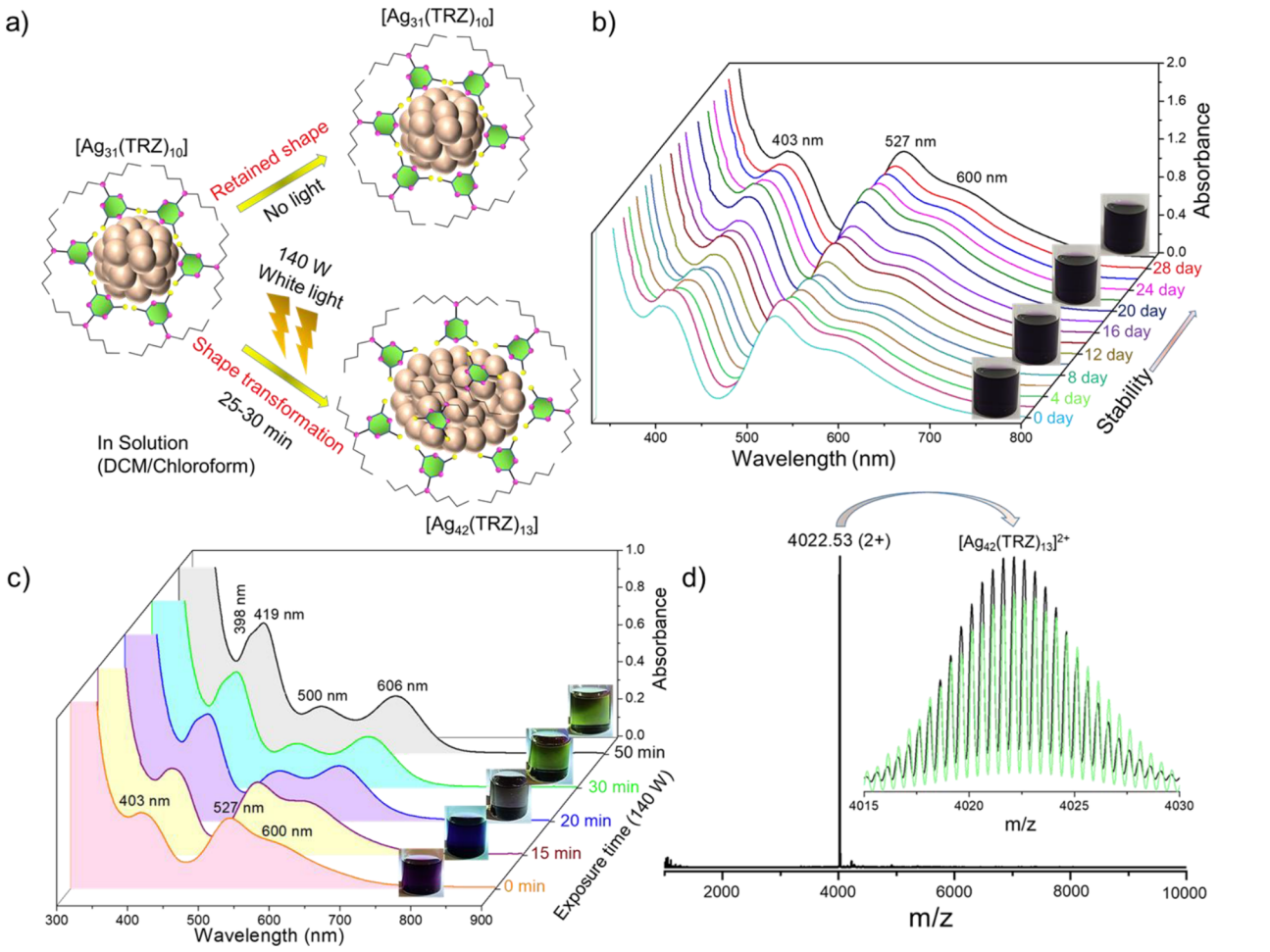

Figure 3. (a) Schematic representation shows light-irradiated conversion of Ag_{31} to Ag_{42} in DCM solution, whereas Ag_{31} remains intact without light irradiation. (b) Time-dependent UV−vis absorption spectra of Ag_{31} show stability for a month without light exposure. (c) UV−vis absorption spectra during the conversion process. The inset shows the photographs of the respective solutions at different time points. Upon further exposure for 120 min, no change was noticed. (d) Positive-ion mode ESI-MS spectrum of as formed Ag_{42} after 30 min of light illumination. Complete conversion of the parent cluster is noticed.

both mono- and dianionic species of the cluster (Figure S5). Furthermore, a peak at 3094.41 (charge state 2−) corresponding to Cs^+ attachment with the trianionic cluster, i.e., $[Ag_{31}(TRZ)_{10}]^{3-}$, was detected. Collectively, these findings provide evidence for the coexistence of multianionic charge states of the cluster, with a dianionic cluster as the major species in solution.

To gain additional insight into the molecular composition of the cluster, we have performed collision energy-dependent fragmentation studies upon isolating the parent dianionic species at m/z 3024.02 (shown in Figure 2a). No fragmentation of the parent peak was observed up to CE 10 (in an instrument unit). Upon further increasing the collision energy from CE 10 to 35, we observed two new peaks with a monoanionic charge state at m/z 5777.72 and 5399.82. The mass losses of 270 and 648 amu represent the fragmentation of TRZ and $Ag(TRZ)_2$, respectively, from the parent $[Ag_{31}(TRZ)_{10}]$ NC. Therefore, the two peaks at 5777.72 and 5399.82 are assigned to the molecular formulae, $[Ag_{31}(TRZ)_9]^-$ and $[Ag_{30}(TRZ)_8]^-$, respectively. Upon further increasing the collision energy to CE 70, a few additional peaks were observed at m/z 4913.13, 4157.06, and 3779.24. These new fragments are assigned as $[Ag_{28}(TRZ)_7]^-$, $[Ag_{26}(TRZ)_5]^-$, and $[Ag_{25}(TRZ)_4]^-$. We have also observed several new fragmented peaks along with these prominent peaks at CE 60. The major fragmented peaks at m/z 3019.84, 2633.04, 2351.79, 2320.04, 2120.32, 2061.42, 1836.29, 1779.93, 1350.52, 1232.74, and 1031.01 are assigned to the compositions, $[Ag_{14}S_5(TRZ)_5]^-$, $[Ag_{11}S_3(TRZ)_5]^-$, $[Ag_9S(TRZ)_5]^-$, $[Ag_9(TRZ)_5]^-$, $[Ag_9S_2(TRZ)_4H_5]^-$, $[Ag_{11}S_2(TRZ)_3]^-$, $[Ag_{12}(TRZ)_2H_2]^-$, $[Ag_9(TRZ)_3]^-$, $[Ag_5(TRZ)_3H]^-$, $[Ag_8S_3(TRZ)H_4]^-$, and $[Ag_7(TRZ)H_6]^-$, respectively (shown in Figures S6 and S7). Altogether, the losses of different Ag and TRZ fragments during collision-induced dissociation studies confirmed the molecular composition of Ag_{31}.

The Ag_{31} cluster was further characterized by scanning transmission electron microscopy (STEM). The STEM micrograph in Figure 2b shows ultrasmall particles with a dimension of <2 nm. The ^1H NMR chemical shifts at 3.54, 1.56, 1.32, and 0.89 ppm of the free ligands were shifted to 3.39, 1.43, 1.17, and 0.81 ppm in the cluster (Figures S8 and S9). The broad spectral features of the Ag_{31} cluster are due to the large electron density of the silver core. Fourier transform infrared (FT-IR) spectroscopy also depicts the binding of the TRZ ligand on the cluster. Figure S10 shows the comparative IR spectra of the free TRZ-H_2 ligand and the Ag_{31} cluster. The C−H stretching peak at 2950 cm^{-1} remains at the same

https://doi.org/10.1021/acs.chemmater.3c01293
Chem. Mater. 2023, 35, 7020−7031

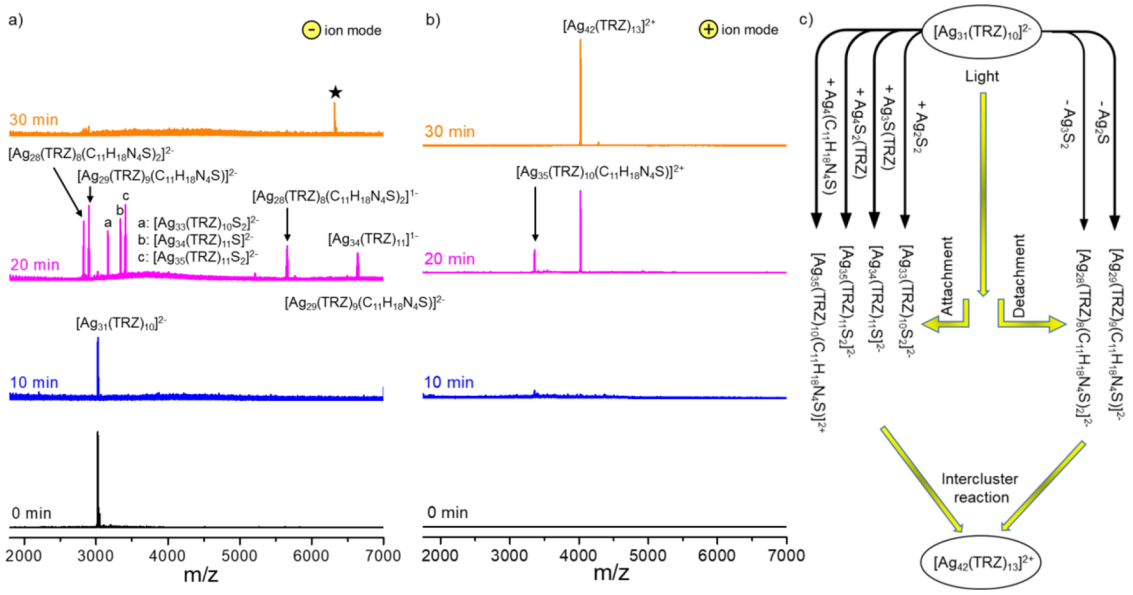

Figure 4. Time-dependent MS spectra showing the formation of intermediate NCs in (a) negative- and (b) positive-ion modes during the conversion of Ag_{31} to Ag_{42}. * indicates some complex species. (c) Schematic illustration of the intermediate species formed during the conversion process.

position for the cluster, which suggests that the butyl chains remain unaffected. The C═N stretching peaks at 1599 and 1536 cm^{-1} for the TRZ-H_2 ligand were shifted to 1513 and 1478 cm^{-1} due to the close proximity of triazine moiety. The sharpness of the C−N stretching band was reduced, while the peak remained at the same position (1126 cm^{-1}). X-ray photoelectron spectroscopy (XPS) was performed on the Ag_{31} cluster, and the data are shown in Figure S11. The survey scan shows the presence of the respective elements, i.e., Ag, S, C, and N, originating from the metal and ligands. We could not successfully prepare single crystals suitable for X-ray diffraction. The as-prepared violet powder shows weak X-ray diffraction features due to poor crystallinity (Figure S12). To investigate the thermal stability of the cluster, we measured its thermogravimetric (TG) profile. TG measurement shows thermal stability of the cluster without having any mass losses up to ∼200 °C (shown in Figure 2c).

Light-Triggered Intercluster Conversion. Despite ambient stability and thermal robustness, we observed the conversion of Ag_{31} to other clusters upon photoirradiation, which is visible by the change in the color of the solution. Figure 3a shows the schematic representation of the light-illuminated conversion of Ag_{31} to Ag_{42}, whereas no conversion was observed for the same cluster without light irradiation. We monitored the UV−vis absorption spectra of the cluster in DCM for an interval of 2 days and observed identical absorbance features after 30 days without any light irradiation (Figure 3b). Ambient stability of the cluster was also observed in chloroform solution (Figure S13). However, white light irradiation (Xe arc lamp, 140 W) results in a visible change of color from violet to green after 30 min of irradiation (Figure 3c). UV−vis absorption measurement showed that the green product has absorption bands centered at 398, 419, 500, and 606 nm in a characteristic pattern, which indicates the formation of a new cluster. Time-dependent UV−vis measurements showed three characteristic bands at 403, 527, and 600 nm up to 15 min of light irradiation, which suggests that Ag_{31} remains intact in the solution. Further 20−25 min of irradiation resulted in a grayish intermediate solution, which was converted to a green-colored solution within 5−10 min. The absorption features of the gray and green solutions are nearly similar. After continuous light exposure up to 60 min, absorption features remained the same, confirming that the green solution is the final product in the conversion process.

The molecular composition of the end product and the intermediate species formed during such a conversion process were monitored using HR-ESI-MS studies. Time-dependent MS studies showed the appearance of the peak at m/z 3024.02 (charge state 2−) after 15 min of light exposure (Figure 4a,b), which suggests the presence of Ag_{31} cluster in solution up to 15 min. Additional peaks were not observed in the positive-ion mode. The MS data of the grayish intermediate species (formed after 20−25 min of light exposure) show two new peaks at m/z 3358.79 and 4022.53 in the positive-ion mode with a charge state of 2+. These peaks are assigned to $[Ag_{35}(TRZ)_{10}(C_{11}H_{18}N_4S)]^{2+}$ and $[Ag_{42}(TRZ)_{13}]^{2+}$. There are multiple new peaks at m/z 2830.10, 2899.97, 3164.34, 3337.20, and 3407.16 with 2− charge state, which are assigned as $[Ag_{28}(TRZ)_8(C_{11}H_{18}N_4S)_2]^{2-}$, $[Ag_{29}(TRZ)_9(C_{11}H_{18}N_4S)]^{2-}$, $[Ag_{33}(TRZ)_{10}S_2]^{2-}$, $[Ag_{34}(TRZ)_{11}S]^{2-}$, and $[Ag_{35}(TRZ)_{11}S_2]^{2-}$, respectively. The green-colored end product has a single peak at m/z 4022.53, with dipositive charge state with the composition as $[Ag_{42}(TRZ)_{13}]^{2+}$, and theoretical isotopic distribution matches well with the experimental spectrum (Figure 3d). No other species were observed throughout the MS spectrum. Also, data collected in the negative-ion mode show no peaks, which suggests the complete conversion of Ag_{31} to Ag_{42} (Figure S14). Therefore, light illumination resulted in clusters with lower and higher nuclearities, and the intercluster reaction between these species (summarized in Figure 4c) resulted in Ag_{42} as an end product. Light-induced growth was observed for a gold NC upon reorganization of the fragmented species arising from light exposure.[65]

Collision energy-dependent fragmentation studies were performed to understand the structural skeleton of the Ag_{42}

https://doi.org/10.1021/acs.chemmater.3c01293
Chem. Mater. 2023, 35, 7020−7031

NC (Figure 5). On increasing the CE from 0 to 50, no fragmentation of the parent cluster was observed. Further

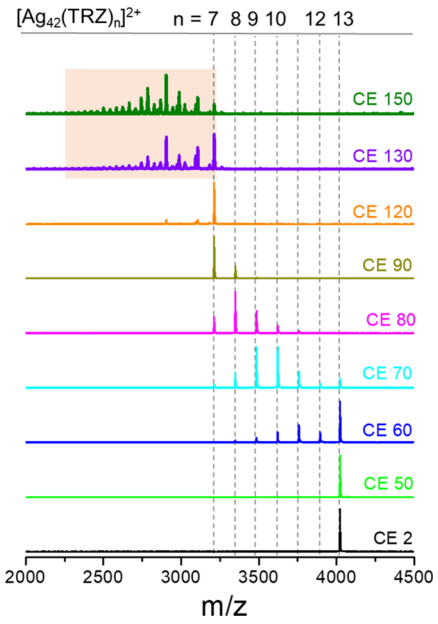

Figure 5. Collision energy-dependent MS/MS fragmentation spectra of Ag_{42}. Sequential TRZ detachment of up to six ligands was observed upon increasing the collision energy. An expanded view of the highlighted region with peak assignments is shown in the Supporting Information.

increasing the collision energy to CE 60, we observed the appearance of five new peaks at m/z 3887.46, 3752.33, 3617.35, 3482.42, and 3347.53 with a dipositive charge state. The sequential mass losses of m/z 270 indicate loss of TRZ ligands from the cluster. Upon further increasing CE to 120, we observed losses of six TRZ fragments from the cluster. Increasing the CE beyond 120 leads to the fragmentation of the metal core of the cluster. Detailed analyses of the molecular composition of these fragments in the lower mass range are presented in Figure S15. Fragmentation of TRZ ligands were also observed.

We have observed a similar type of light-activated conversion in chloroform solution, confirmed through UV−vis absorption and MS studies (shown in Figure S16). The identical absorption features (shown in Figure S17) up to 24 days in DCM and chloroform solutions, respectively, indicate the stability of Ag_{42} in ambient conditions. XPS and IR studies further confirm the binding of the TRZ ligands. The XPS survey spectrum shows the presence of the expected elements, i.e., Ag, S, C, and N in Ag_{42} (Figure S18). The binding energy of 368.4 and 374.4 eV represents the $3d_{5/2}$ and $3d_{3/2}$ of metallic silver (0). Spectral fitting of the C 1s region shows three peaks at 285.1, 286.1, and 287.6 eV due to C−C, C−N, and C═N bonding of TRZ ligands. Deconvolution of the N 1 s region shows two peaks at 398.7 and 400.1 eV due to C−N and C═N bonding, respectively. FT-IR studies (shown in Figure S19) further confirm the binding of TRZ ligands with the cluster. TEM investigation reveals the appearance of ultrasmall Ag_{42}, having an average particle diameter of 1.93 ± 0.12 nm (shown in Figure S20).

The intercluster conversion kinetics depends on the lamp power and concentration of the cluster. We have studied the conversion process using different lamp powers, i.e., 100, 140, and 180 W having the same concentration (1 mg/mL). Comparative UV−vis measurements (shown in Figure S21) reveal a slowdown (∼ 40 min) of the conversion kinetics under the lamp power of 100 W, whereas the conversion took ∼20 min under the 180 W lamp. Similarly, we measured the conversion kinetics at 140 W at varying cluster concentrations of 1, 3, and 5 mg/mL (shown in Figure S22). The conversion took 30 min for 1 mg/ ml and 50 and 70 min for 3 and 5 mg/ mL concentrations, respectively. The reduction of the absorbance of Ag_{42} in comparison to Ag_{31} also suggests the reduction of the number of particles upon such a photoconversion process. Furthermore, we have studied the effect of light activation in the solid state. A cluster film was prepared on a glass slide upon drop casting 3 mg of Ag_{31} upon dissolution in DCM. Time-dependent UV−vis absorption studies of the light-exposed thin film showed identical spectral bands up to 210 min of light exposure (lamp power 140 W) (Figure S23). Therefore, this light-activated intercluster conversion is a solution-state phenomenon. The interactions between clusters through long butyl chains on each TRZ ligand promote the dissociation and aggregation reaction pathways. The present finding provides new insight into the ligand's effect on light-induced intercluster conversion. Our earlier studies demonstrated the light-induced conversion of *ortho*-carborane 1, 2-dithiol, and triphenylphosphine coprotected silver NC in DCM solution.[66] The presence of long butyl chains and nitrogen with multiple binding sites on TRZ ligands facilitates short-range intercluster interactions in solution, playing a significant role in increasing the nuclearity of the cluster.

To understand the electronic stability, we have calculated the valence electrons of these clusters using the electron counting formula as $(N\nu-M-Z)$, where N = number of metal atoms, ν = atomic valence of the metal atom, M = number of ligands, and Z = overall charge.[67−69] $[Ag_{31}(TRZ)_{10}]^{2-}$ and $[Ag_{31}(TRZ)_{10}]^{1-}$ have an electron count of 13e (31−20 + 2) and 12e (31−20 + 1), respectively. This cluster showed photosensitive behaviors, probably due to the lack of a close shell superatomic electronic configuration. On the other hand, the valence electron for the $[Ag_{42}(TRZ)_{13}]^{2+}$ cluster is 14e (42−26−2).

Understanding the Intercluster Conversion through Photoelectrochemical Studies. To understand the photoactivated conversion process, we have measured the open-circuit potential (OCP) of Ag_{31} solution (in DCM) during light illumination conditions. This experiment refers to previously studied measurements (by Bard et al.) of single nanoparticle collisions by OCP and other electrochemical techniques.[70−73] We used 0.2 M TBAF as the electrolyte during the measurement to enhance ionic conductivity of the solution. The OCP measurements of Ag_{31} solution (concentration of 1 mg/mL) show a gradual rise in potential after light exposure. Continuous light exposure up to ∼3000 s shows three different kinetics during this conversion process (Figure 6a). The rate of potential enhancement is 6.56×10^{-4} V/s for an interval of ∼130 s, and this indicates the initial conversion step. This rapid potential enhancement compared to other steps is due to the enhanced Brownian motion of the Ag_{31} cluster. The second and third kinetics took ∼1250 and ∼1400 s, with the rate of OCP enhancement being 7.58×10^{-5} and 1.98×10^{-5} V/s, respectively. Electrons generated from the negatively charged Ag_{31} are probably responsible for this light-activated enhancement of potential. As these electrons are

https://doi.org/10.1021/acs.chemmater.3c01293
Chem. Mater. 2023, 35, 7020−7031

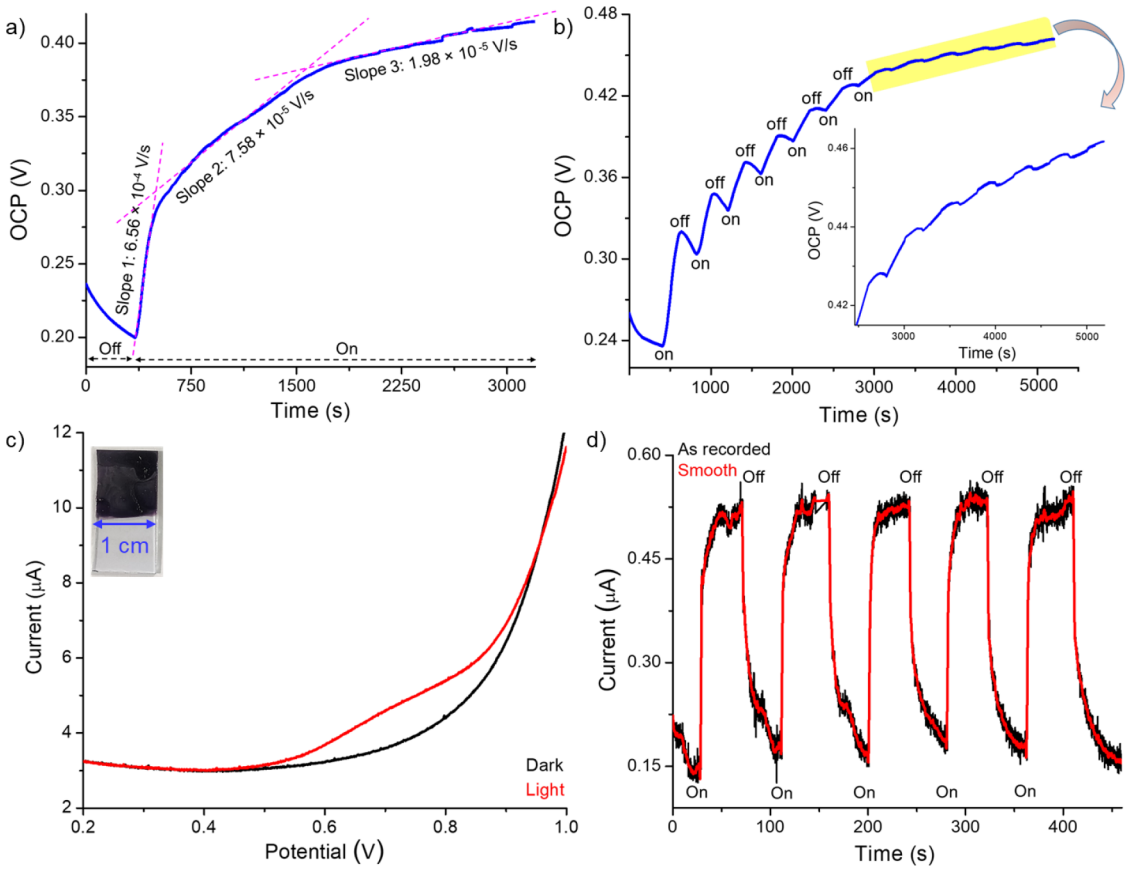

Figure 6. (a) OCP measurement of Ag_{31} in the presence of 0.2 M TBAF solution in DCM (conc. 1 mg/mL) during continuous light illumination (140 W). (b) OCP profile of Ag_{31} during a sequential light on and off cycle. Light exposure time is 200 s in each step. (c) Electrochemical LSV current−voltage (I−V) characteristics of Ag_{31} in the presence of 0.01 M Na_2SO_4 solution. The inset shows a photograph of an ITO electrode coated with Ag_{31}. (d) Chronoamperometric measurement of the Ag_{31} film at 0.72 V demonstrated a reversible photocurrent response.

generated in their respective solutions, we believe that they are solvated. Propagating solvated electrons upon photoexcitation was also observed for various gold and silver nanoparticles.[74−76] To understand the role of the cluster, a control OCP measurement was performed using the same electrolyte solution without cluster, and there was no change in OCP response under the photoillumination condition (Figure S24). Independent OCP measurements using cluster concentrations of 1, 2, and 3 mg/mL show similar first kinetic step (∼130 s) for all concentrations, whereas the time taken for the second kinetic step increases from ∼1250 s for 1 mg/mL to 2000 and 3000 s for 2 and 3 mg/mL clusters, respectively (shown in Figure S25). All these measurements suggest that the second conversion step is the rate-determining step for this conversion process. Increasing concentration took more time to complete the conversion, which is correlated with the concentration-dependent UV−vis absorption studies (shown in Figure S22). Rather than continuous exposure of light, a stepwise light exposure cycle (time interval for each on−off step is 200 s) shows a gradual reduction of the OCP photoresponse (shown in Figure 6b). After ∼3000 s of stepwise light exposure, photosensitivity reduces significantly since the formed Ag_{42} is less photoactive than Ag_{31}. The newly formed intermediate clusters, monitored through MS studies, along with the solvated electrons are responsible for making the Ag_{42} cluster. An independent cyclic voltammetry measurement also shows the emergence of photogenerated electrons for Ag_{31} cluster in DCM solution (concentration of 1 mg/mL with 0.2 M TBAF) (Figure S26a). On the other hand, the presynthesized Ag_{42} cluster remains photosilent in similar electrochemical conditions (shown in Figure S26b).

Considering the light sensitivity of Ag_{31} cluster, electrochemical photocurrent measurements in the solid state were performed upon preparing a thin layer of clusters on an indium tin oxide (ITO) working electrode (active surface area 1 cm^2). Photocurrent measurements were performed using 0.01 M aqueous Na_2SO_4 electrolyte in the presence of Pt wire as a counter electrode and Ag/AgCl as a reference electrode. Linear sweep voltammetry (LSV) measurements for Ag_{31} (Figure 6c) showed a positive photocurrent response in the potential range of 0.5−0.9 V upon light illumination. Furthermore, chronoamperometric measurement shows a positive photocurrent response of ∼0.38 μA at a bias voltage of 0.72 V. The photocurrent response was reversible up to five cycles (Figure 6d). Bare ITO electrodes did not impart any photocurrent response in the same condition (Figure S27). Photogenerated electrons of Ag_{31} were transferred to the ITO electrode, which exhibited a photocurrent in the solid state. Intercluster collisions between these charged species are interrupted in the solid state. However, dynamic motions in solution and subsequent intercluster collision are responsible for such intercluster conversion.

Effect on Optical Emission. We have measured the emission properties of both the clusters in their respective solutions in DCM. Ag_{31} shows no visible luminescence under 365 nm UV light, as shown in the inset of Figure 7a. PL

https://doi.org/10.1021/acs.chemmater.3c01293
Chem. Mater. 2023, 35, 7020−7031

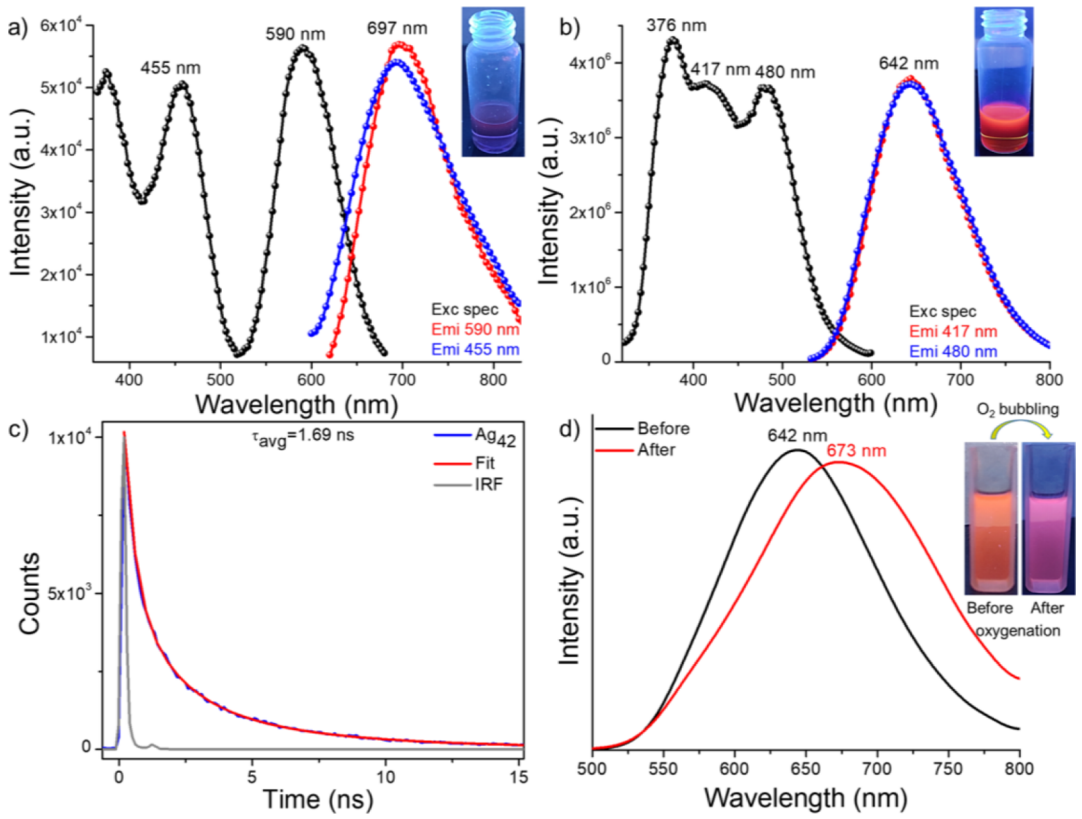

Figure 7. (a) PL excitation and emission spectra of Ag_{31} show a weak NIR-I emission. The inset shows the respective cluster under UV light. (b) PL excitation and emission spectra of Ag_{42} show bright red luminescence. The inset shows an image of the cluster under UV light. (c) Fluorescence decay profile of Ag_{42}. (d) Emission spectra of Ag_{42} before and after oxygenation. The excitation wavelength is 480 nm. The inset shows images of the Ag_{42} cluster under UV light.

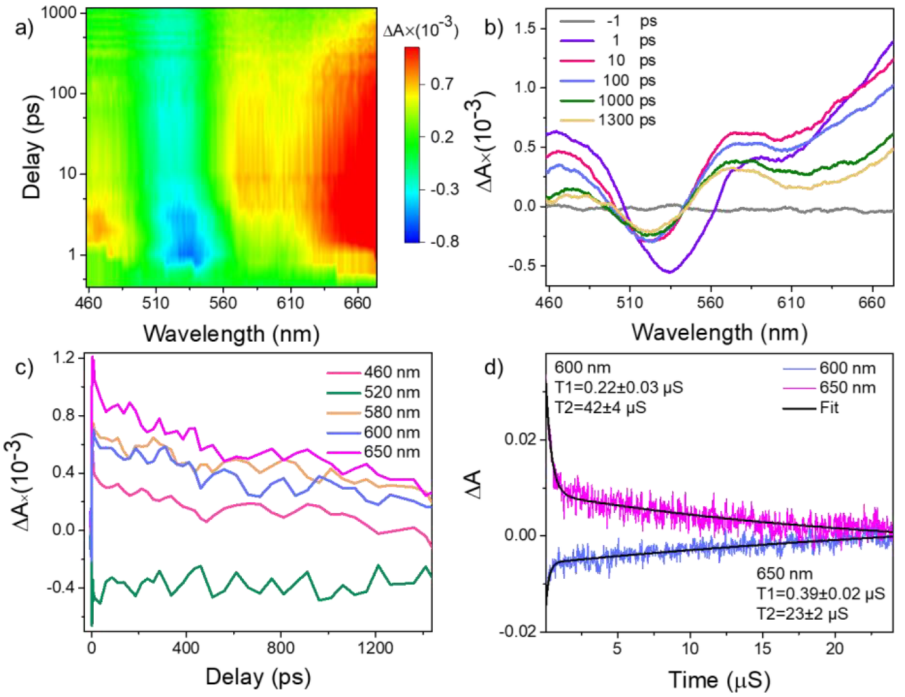

Figure 8. (a) Contour plot of the fs-TA spectrum of Ag_{31} NC, where the pump excitation was at 400 nm. (b) Spectral evolution TA as a function of time delay. (c) Kinetic decay traces of ESA and GSPB signals. (d) Nanosecond time evolution spectral profile measured by laser flash photolysis.

spectral measurement shows a weak emission at 697 nm in the NIR-I window, using excitations at 455 and 590 nm. On the other hand, the Ag_{42} has a bright red luminescence under a 365 nm UV lamp (shown in the inset of Figure 7b). The emission maximum was centered at 642 nm upon photoexcitation at 376, 417, and 480 nm. The emissive lifetime of 1.69 ns in its

https://doi.org/10.1021/acs.chemmater.3c01293
Chem. Mater. 2023, 35, 7020−7031

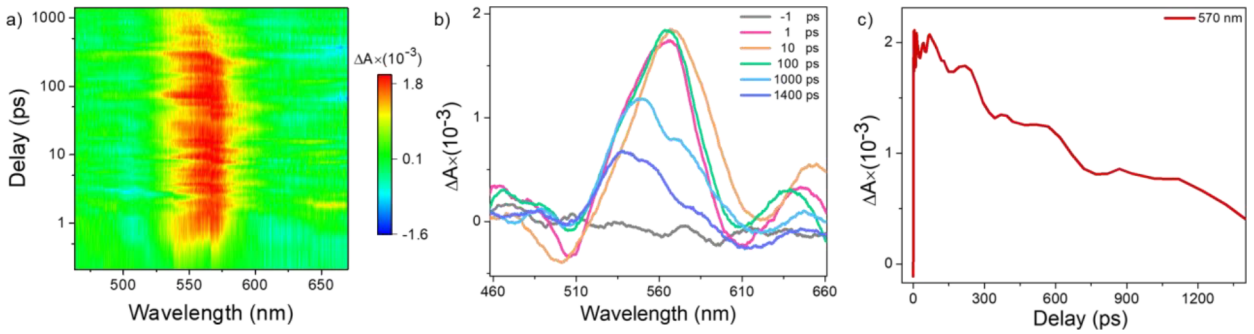

Figure 9. (a) fs-TA contour map of Ag_{42}, where the pump excitation was at 400 nm. (b) Time evolution of the TA spectra of Ag_{42}. (c) Selected kinetic decay traces for the 570 nm ESA features.

DCM solution (Figure 7c) suggests fluorescence emission originating from the singlet excited state. The expansion of the emissive band gap (0.15 eV) and enhancement of the emission intensity for the Ag_{42} cluster are probably due to the enhanced symmetry of the ligand distribution around the cluster core, which promotes enhanced interfacial charge transfer.

Although there is no significant visible color change of the cluster in its solid state, we observed double emission bands centered at 649 and 740 nm, where 740 nm is the primary emission band (Figure S28). Intercluster interaction in the solid state is probably the reason behind these low-energy emission features. After oxygen bubbling, there is no significant emission quenching, confirming that the emission originated from a singlet state. However, we observed a visible color change from orange to purple after oxygen bubbling (30−35 min). PL measurement (Figure 7d) shows a 642 nm peak that shifted to 673 nm after oxygen exposure. Although the singlet excited state is not quenched by oxygen, the interactions between the Ag_{42} cluster and oxygen lead to the stabilization of the excited state. Identical UV−vis absorption features (shown in Figure S29) of the oxygenated sample suggest the structural stability of the Ag_{42} cluster.

Comparative Excited-State Electron Dynamics. We conducted femtosecond transient absorption (fs-TA) and nanosecond laser flash-photolysis (ns-LFP) studies to visualize the excited-state carrier dynamics of these clusters. In our measurements, we excited the sample in DCM solution with a 120 fs laser pulse at 400 nm, and the resulting change in the system was monitored by time-delayed broad band pulses of 460−670 nm range. Specific instrumentation details can be found in the Supporting Information. The fs-TA signals of Ag_{31} are plotted in Figure 8. The contour maps of Ag_{31} consist of ground state photobleaching (GSPB) bands at 520 and 610 nm, along with three excited -state absorption (ESA) features (yellow and red colors represent a positive signal) at 470, 580, and 650 nm (Figure 8a).

For better quantification, the spectral cross-section at the selected time delay is shown in Figure 8b. The figure shows that the primary photobleach is at 520 nm, which is the position of optical absorption (527 nm) manifested in the form of a negative signal. However, the 610 nm GSPB band is visible only in the downhill region in the ESA band. These photobleach signals arise due to the phase-space filling of excited-state carriers formed by pump excitation, and ESA is due to the transitions of these carriers into elevated excited-energy states. Here, it is interesting to see that among all these features, photobleach (in the region of 520 and 610 nm) and ESA (470 and 670 nm) have the same type of time evolution but relatively different and correlated electron dynamics compared to the ESA of 580 nm (Figure 8c). The features of 520, 620, 470, and 670 nm build up immediately after photoexcitation within the same time period of 0.5 ps and then exhibit an early decay.

On the other hand, ESA of 580 nm rises slowly and builds up in the decay duration. This behavior suggests that an ESA of 580 nm arises after the early decay of all other features. For quantification of this ultrashort-time behavior, the temporal profile for the early time is shown Figure S30. By fitting the decay with of the single exponential function, we found the decay constant of 3.6 ± 0.3 and 3.5 ± 0.5 ps. This type of ultrafast electronic behavior was also observed for the gold and silver NCs and assigned to the internal conversion from (LUMO+n) to LUMO states.[77−79] These studies suggest that the observed electron dynamics of the excited state can be linked to two different processes. The first fast relaxation is due to internal conversion, and the subsequent slow component is due to the relaxation within the ground state. Further, the excited-state carriers do not relax completely, suggesting a long lifetime. Therefore, to determine the decay kinetics of relaxation to the ground state, ns-LFP of Ag_{31} was performed (Figure 8d), revealing a microsecond-long lifetime for the cluster.

TA spectral features of Ag_{42} are plotted in Figure 9, where we see weak GSPB bands at 510 and 606 nm and prominent excited-state absorption bands at 465, 560, and 650 nm. Although the spectral features of both the clusters are nearly similar, their lifetimes are contrastingly different. Temporal evolution of TA in Figure 9c reveals a ns lifetime compared to the μs lifetime for the parent Ag_{31}.

CONCLUSIONS

In conclusion, we present the first triazine dithiol-protected silver NC, i.e., Ag_{31}, using a triphenylphosphine-assisted metal thiolate coreduction reaction. The UV−vis absorption bands in a characteristic pattern represent the discrete electronic energy levels of the NC. MS measurements and collision energy-dependent fragmentation studies confirm the molecular composition of the cluster with mono- and dianionic charge states. Thermally stable Ag_{31} shows light-triggered size expansion in its solution. The visible color change from violet to green and the changes in the UV−vis spectral features reveal such a light-activated process. MS studies confirm the formation of $[Ag_{42}(TRZ)_{13}]^{2+}$ as an end product through intercluster reactions between intermediate clusters with lower and higher nuclearities. The PL spectral measurements showed that the Ag_{31} is weakly NIR emissive, with an emission

https://doi.org/10.1021/acs.chemmater.3c01293
Chem. Mater. 2023, 35, 7020−7031

maximum at 697 nm, whereas the Ag_{42} is intensely red emissive (maximum at 642 nm). The photoconducting Ag_{31} shows light-irradiated enhancement of OCP in photoelectrochemical conditions. The formation of light-activated solvated electrons might be triggering this conversion process. The femtosecond and nanosecond ultrafast TA studies reveal that the stable excited-state carriers of Ag_{31} (lifetime in the μs range) got converted to Ag_{42}, having unstable carriers with ns lifetime. Altogether, these studies showed an unusual size evolution of a silver nanocluster triggered by light.

■ ASSOCIATED CONTENT

Supporting Information

The Supporting Information is available free of charge at https://pubs.acs.org/doi/10.1021/acs.chemmater.3c01293.

Instrumentation details, supplementary UV−vis, PL, MS spectra, NMR, IR, XPS, and TEM characterization of Ag_{31} and Ag_{42} nanoclusters, and details of intercluster conversion measured through UV−vis and photoelectrochemical measurements (PDF)

■ AUTHOR INFORMATION

Corresponding Authors

Kumaran Nair Valsala Devi Adarsh − *Department of Physics, Indian Institute of Science Education and Research Bhopal, Bhopal 462066, India;* orcid.org/0000-0002-6337-6545; Email: adarsh@iiserb.ac.in

Robin H. A. Ras − *Department of Applied Physics, School of Science, Aalto University, 02150 Espoo, Finland;* orcid.org/0000-0002-2076-242X; Email: robin.ras@aalto.fi

Thalappil Pradeep − *DST Unit of Nanoscience (DST UNS) and Thematic Unit of Excellence (TUE), Department of Chemistry, Indian Institute of Technology Madras, Chennai 600036, India;* orcid.org/0000-0003-3174-534X; Email: pradeep@iitm.ac.in

Authors

Arijit Jana − *DST Unit of Nanoscience (DST UNS) and Thematic Unit of Excellence (TUE), Department of Chemistry, Indian Institute of Technology Madras, Chennai 600036, India*

Wakeel Ahmed Dar − *DST Unit of Nanoscience (DST UNS) and Thematic Unit of Excellence (TUE), Department of Chemistry, Indian Institute of Technology Madras, Chennai 600036, India*

Sourav Kanti Jana − *DST Unit of Nanoscience (DST UNS) and Thematic Unit of Excellence (TUE), Department of Chemistry, Indian Institute of Technology Madras, Chennai 600036, India;* orcid.org/0000-0001-5772-7022

Ajay Kumar Poonia − *Department of Physics, Indian Institute of Science Education and Research Bhopal, Bhopal 462066, India;* orcid.org/0000-0002-5551-7299

Vivek Yadav − *DST Unit of Nanoscience (DST UNS) and Thematic Unit of Excellence (TUE), Department of Chemistry, Indian Institute of Technology Madras, Chennai 600036, India*

Jayoti Roy − *DST Unit of Nanoscience (DST UNS) and Thematic Unit of Excellence (TUE), Department of Chemistry, Indian Institute of Technology Madras, Chennai 600036, India*

Sourov Chandra − *Department of Applied Physics, School of Science, Aalto University, 02150 Espoo, Finland;* orcid.org/0000-0003-0129-4242

Complete contact information is available at: https://pubs.acs.org/10.1021/acs.chemmater.3c01293

Notes

The authors declare no competing financial interest.

■ ACKNOWLEDGMENTS

The authors acknowledge the support of the Department of Science and Technology (DST), Govt. of India. A.J. thanks the IIT Madras for his research fellowship. We thank the Sophisticated Analytical Instruments Facility (SAIF), IIT Madras, for thermogravimetric measurements. T.P. acknowledges funding from the Centre of Excellence on Molecular Materials and Functions under the Institution of Eminence scheme of IIT Madras. K.N.V.D.A. gratefully acknowledges the Science and Engineering Research Board (SERB) for the grant CRG/2019/002808. This work was also supported by the Academy of Finland Center of Excellence Program (2022-2029) in Life-Inspired Hybrid Materials (LIBER) project number 346109.

■ DEDICATION

This article is dedicated to Prof. K. Vidyasagar on the occasion of his 65th birthday.

■ REFERENCES

(1) Jin, R.; Zeng, C.; Zhou, M.; Chen, Y. Atomically Precise Colloidal Metal Nanoclusters and Nanoparticles: Fundamentals and Opportunities. *Chem. Rev.* **2016**, *116*, 10346−10413.

(2) Chakraborty, I.; Pradeep, T. Atomically Precise Clusters of Noble Metals: Emerging Link between Atoms and Nanoparticles. *Chem. Rev.* **2017**, *117*, 8208−8271.

(3) Pradeep, T., Ed.; *Atomically Precise Metal Nanoclusters*; Elsevier: Amsterdam, 2023; pp 1−643.

(4) Jana, A.; Kini, A. R.; Pradeep, T. Atomically Precise Clusters: Chemical Evolution of Molecular Matter at the Nanoscale. *AsiaChem Mag.* **2023**, *3*, 56−65.

(5) Jena, P.; Sun, Q. Super Atomic Clusters: Design Rules and Potential for Building Blocks of Materials. *Chem. Rev.* **2018**, *118*, 5755−5870.

(6) Luo, X. M.; Li, Y. K.; Dong, X. Y.; Zang, S. Q. Platonic and Archimedean Solids in Discrete Metal-Containing Clusters. *Chem. Soc. Rev.* **2023**, *52*, 383−444.

(7) Chen, T.; Lin, H.; Cao, Y.; Yao, Q.; Xie, J. Interactions of Metal Nanoclusters with Light: Fundamentals and Applications. *Adv. Mater.* **2022**, *34*, No. 2103918.

(8) Kang, X.; Zhu, M. Tailoring the Photoluminescence of Atomically Precise Nanoclusters. *Chem. Soc. Rev.* **2019**, *48*, 2422−2457.

(9) Luo, Z.; Castleman, A. W.; Khanna, S. N. Reactivity of Metal Clusters. *Chem. Rev.* **2016**, *116*, 14456−14492.

(10) Han, Z.; Dong, X.; Luo, P.; Li, S.; Wang, Z.; Zang, S.; Mak, T. C. W. Ultrastable Atomically Precise Chiral Silver Clusters with More than 95% Quantum Efficiency. *Sci. Adv.* **2020**, *6*, No. eaay0107.

(11) Yang, H.; Lei, J.; Wu, B.; Wang, Y.; Zhou, M.; Xia, A.; Zheng, L.; Zheng, N. Crystal Structure of a Luminescent Thiolated Ag Nanocluster with an Octahedral Ag_6^{4+} Core. *Chem. Commun.* **2013**, *49*, 300−302.

(12) Cerretani, C.; Kanazawa, H.; Vosch, T.; Kondo, J. Crystal Structure of a NIR-Emitting DNA-Stabilized Ag_{16} Nanocluster. *Angew. Chem., Int. Ed.* **2019**, *58*, 17153−17157.

(13) Jana, A.; Unnikrishnan, P. M.; Poonia, A. K.; Roy, J.; Jash, M.; Paramasivam, G.; Machacek, J.; Adarsh, K. N. V. D.; Base, T.; Pradeep, T. Carboranethiol-Protected Propeller-Shaped Photoresponsive Silver Nanomolecule. *Inorg. Chem.* **2022**, *61*, 8593−8603.
(14) Joshi, C. P.; Bootharaju, M. S.; Alhilaly, M. J.; Bakr, O. M. $[Ag_{25}(SR)_{18}]^-$: The "Golden"Silver Nanoparticle. *J. Am. Chem. Soc.* **2015**, *137*, 11578−11581.
(15) AbdulHalim, L. G.; Bootharaju, M. S.; Tang, Q.; Del Gobbo, S.; AbdulHalim, R. G.; Eddaoudi, M.; Jiang, D. E.; Bakr, O. M. $Ag_{29}(BDT)_{12}(TPP)_4$: A Tetravalent Nanocluster. *J. Am. Chem. Soc.* **2015**, *137*, 11970−11975.
(16) Guan, Z. J.; Zeng, J. L.; Nan, Z. A.; Wan, X. K.; Lin, Y. M.; Wang, Q. M. Thiacalix[4]Arene: New Protection for Metal Nanoclusters. *Sci. Adv.* **2016**, *2*, No. e1600323.
(17) Bodiuzzaman, M.; Ghosh, A.; Sugi, K. S.; Nag, A.; Khatun, E.; Varghese, B.; Paramasivam, G.; Antharjanam, S.; Natarajan, G.; Pradeep, T. Camouflaging Structural Diversity: Co-Crystallization of Two Different Nanoparticles Having Different Cores but the Same Shell. *Angew. Chem., Int. Ed.* **2019**, *58*, 189−194.
(18) Yuan, S. F.; Xu, C. Q.; Liu, W. D.; Zhang, J. X.; Li, J.; Wang, Q. M. Rod-Shaped Silver Supercluster Unveiling Strong Electron Coupling between Substituent Icosahedral Units. *J. Am. Chem. Soc.* **2021**, *143*, 12261−12267.
(19) Alhilaly, M. J.; Bootharaju, M. S.; Joshi, C. P.; Besong, T. M.; Emwas, A. H.; Juarez-Mosqueda, R.; Kaappa, S.; Malola, S.; Adil, K.; Shkurenko, A.; Häkkinen, H.; Eddaoudi, M.; Bakr, O. M. $[Ag_{67}(SPhMe_2)_{32}(PPh_3)_8]^{3+}$: Synthesis, Total Structure, and Optical Properties of a Large Box-Shaped Silver Nanocluster. *J. Am. Chem. Soc.* **2016**, *138*, 14727−14732.
(20) Song, Y.; Lambright, K.; Zhou, M.; Kirschbaum, K.; Xiang, J.; Xia, A.; Zhu, M.; Jin, R. Large-Scale Synthesis, Crystal Structure, and Optical Properties of the $Ag_{146}Br_2(SR)_{80}$ Nanocluster. *ACS Nano* **2018**, *12*, 9318−9325.
(21) Yang, H.; Wang, Y.; Chen, X.; Zhao, X.; Gu, L.; Huang, H.; Yan, J.; Xu, C.; Li, G.; Wu, J.; Edwards, A. J.; Dittrich, B.; Tang, Z.; Wang, D.; Zheng, N. Plasmonic Twinned Silver Nanoparticles with Molecular Precision. *Nat. Commun.* **2016**, *7*, 12809.
(22) Liu, Y.; Chai, X.; Cai, X.; Chen, M.; Jin, R.; Ding, W.; Zhu, Y. Central Doping of a Foreign Atom into the Silver Cluster for Catalytic Conversion of CO_2 toward C−C Bond Formation. *Angew. Chem., Int. Ed.* **2018**, *57*, 9775−9779.
(23) Pramanik, S.; Bhalla, V.; Kumar, M. Hexaphenylbenzene-Stabilized Luminescent Silver Nanoclusters: A Potential Catalytic System for the Cycloaddition of Terminal Alkynes with Isocyanides. *ACS Appl. Mater. Interfaces* **2015**, *7*, 22786−22795.
(24) (a) Wu, Y.; Wang, D.; Li, Y. Nanocrystals from Solutions: Catalysts. *Chem. Soc. Rev.* **2014**, *43*, 2112−2124. (b) Jin, R.; Li, G.; Sharma, S.; Li, Y.; Du, X. Toward Active-Site Tailoring in Heterogeneous Catalysis by Atomically Precise Metal Nanoclusters with Crystallographic Structures. *Chem. Rev.* **2021**, *121*, 567−648.
(25) Zhang, C.; Guo, Z.; Chen, G.; Zeng, G.; Yan, M.; Niu, Q.; Liu, L.; Zuo, Y.; Huang, Z.; Tan, Q. Green-Emitting Fluorescence Ag Clusters: Facile Synthesis and Sensors for Hg^{2+} Detection. *New J. Chem.* **2016**, *40*, 1175−1181.
(26) Fan, C.; Lv, X.; Liu, F.; Feng, L.; Liu, M.; Cai, Y.; Liu, H.; Wang, J.; Yang, Y.; Wang, H. Silver Nanoclusters Encapsulated into Metal-Organic Frameworks with Enhanced Fluorescence and Specific Ion Accumulation toward the Microdot Array-Based Fluorimetric Analysis of Copper in Blood. *ACS Sens.* **2018**, *3*, 441−450.
(27) Neacşu, V. A.; Cerretani, C.; Liisberg, M. B.; Swasey, S. M.; Gwinn, E. G.; Copp, S. M.; Vosch, T. Unusually Large Fluorescence Quantum Yield for a Near-Infrared Emitting DNA-Stabilized Silver Nanocluster. *Chem. Commun.* **2020**, *56*, 6384−6387.
(28) Díez, I.; Pusa, M.; Kulmala, S.; Jiang, H.; Walther, A.; Goldmann, A. S.; Müller, A. H. E.; Ikkala, O.; Ras, R. H. A. Color Tunability and Electrochemiluminescence of Silver Nanoclusters. *Angew. Chem., Int. Ed. Engl.* **2009**, *48*, 2122−2125.
(29) Chen, L.; Black, A.; Parak, W. J.; Klinke, C.; Chakraborty, I. Metal Nanocluster-based Devices: Challenges and Opportunities. *Aggregate* **2022**, *3*, No. e132.
(30) Jash, M.; Methikkalam, R. R. J.; Bodiuzzaman, M.; Paramasivam, G.; Pradeep, T. Reaction between Ag_{17}^+ and Acetylene Outside the Mass Spectrometer: Dehydrogenation in the Gas Phase. *Chem. Commun.* **2020**, *56*, 15623−15626.
(31) Liu, J. W.; Wang, Z.; Chai, Y. M.; Kurmoo, M.; Zhao, Q. Q.; Wang, X. P.; Tung, C. H.; Sun, D. Core Modulation of 70-Nuclei Core-Shell Silver Nanoclusters. *Angew. Chem., Int. Ed.* **2019**, *58*, 6276−6279.
(32) Desireddy, A.; Conn, B. E.; Guo, J.; Yoon, B.; Barnett, R. N.; Monahan, B. M.; Kirschbaum, K.; Griffith, W. P.; Whetten, R. L.; Landman, U.; Bigioni, T. P. Ultrastable Silver Nanoparticles. *Nature* **2013**, *501*, 399−402.
(33) Bootharaju, M. S.; Joshi, C. P.; Alhilaly, M. J.; Bakr, O. M. Switching a Nanocluster Core from Hollow to Nonhollow. *Chem. Mater.* **2016**, *28*, 3292−3297.
(34) Jana, A.; Chakraborty, P.; Dar, W. A.; Chandra, S.; Khatun, E.; Kannan, M. P.; Ras, R. H. A.; Pradeep, T. Dual Emitting Ag_{35} Nanocluster Protected by 2-Pyrene Imine Thiol. *Chem. Commun.* **2020**, *56*, 12550−12553.
(35) Chakraborty, I.; Kurashige, W.; Kanehira, K.; Gell, L.; Häkkinen, H.; Negishi, Y.; Pradeep, T. $Ag_{44}(SeR)_{30}$: A Hollow Cage Silver Cluster with Selenolate Protection. *J. Phys. Chem. Lett.* **2013**, *4*, 3351−3355.
(36) Bootharaju, M. S.; Dey, R.; Gevers, L. E.; Hedhili, M. N.; Basset, J. M.; Bakr, O. M. A New Class of Atomically Precise, Hydride-Rich Silver Nanoclusters Co-Protected by Phosphines. *J. Am. Chem. Soc.* **2016**, *138*, 13770−13773.
(37) Liu, K. G.; Hu, M. L.; Jiang, D. E.; Gao, X. M.; Liu, T. All-Carboxylate-Protected Superatomic Silver Nanocluster with an Unprecedented Rhombohedral Ag_8 Core. *J. Am. Chem. Soc.* **2020**, *142*, 16905−16909.
(38) Wang, Z.; Alkan, F.; Aikens, C. M.; Kurmoo, M.; Zhang, Z. Y.; Song, K. P.; Tung, C. H.; Sun, D. An Ultrastable 155-Nuclei Silver Nanocluster Protected by Thiacalix[4]Arene and Cyclohexanethiol for Photothermal Conversion. *Angew. Chem., Int. Ed.* **2022**, *61*, No. e202206742.
(39) Zhang, M. M.; Dong, X. Y.; Wang, Z. Y.; Luo, X. M.; Huang, J. H.; Zang, S. Q.; Mak, T. C. W. Alkynyl-Stabilized Superatomic Silver Clusters Showing Circularly Polarized Luminescence. *J. Am. Chem. Soc.* **2021**, *143*, 6048−6053.
(40) Lei, Z.; Wan, X.-K.; Yuan, S.-F.; Guan, Z.-J.; Wang, Q.-M. Alkynyl Approach toward the Protection of Metal Nanoclusters. *Acc. Chem. Res.* **2018**, *51*, 2465−2474.
(41) Su, S. J.; Sasabe, H.; Pu, Y. J.; Nakayama, K. I.; Kido, J. Tuning Energy Levels of Electron-Transport Materials by Nitrogen Orientation for Electrophosphorescent Devices with an Ideal' Operating Voltage. *Adv. Mater.* **2010**, *22*, 3311−3316.
(42) Wang, W.; Hobza, P. Theoretical Study on the Complexes of Benzene with Isoelectronic Nitrogen-Containing Heterocycles. *ChemPhysChem* **2008**, *9*, 1003−1009.
(43) Chandra, S.; Sciortino, A.; Das, S.; Ahmed, F.; Jana, A.; Roy, J.; Li, D.; Liljeström, V.; Jiang, H.; Johansson, L.-S.; Chen, X.; Nonappa; Cannas, M.; Pradeep, T.; Peng, B.; Ras, R. H. A.; Sun, Z.; Ikkala, O.; Mess, F. Gold $Au(I)_6$ Clusters with Ligand-Derived Atomic Steric Locking: Multifunctional Optoelectrical Properties and Quantum Coherence. *Adv. Opt. Mater.* **2023**, *11*, No. 2202649.
(44) Wang, Z.; Su, H. F.; Tan, Y. Z.; Schein, S.; Lin, S. C.; Liu, W.; Wang, S. A.; Wang, W. G.; Tung, C. H.; Sun, D.; Zheng, L. S. Assembly of Silver Trigons into a Buckyball-like Ag_{180} Nanocage. *Proc. Natl. Acad. Sci. U. S. A.* **2017**, *114*, 12132−12137.
(45) Li, Q.; Mosquera, M. A.; Jones, L. O.; Parakh, A.; Chai, J.; Jin, R.; Schatz, G. C.; Gu, X. W. Pressure-Induced Optical Transitions in Metal Nanoclusters. *ACS Nano* **2020**, *14*, 11888−11896.
(46) Yuan, S. F.; Guan, Z. J.; Liu, W. D.; Wang, Q. M. Solvent-Triggered Reversible Interconversion of All-Nitrogen-Donor-Pro-

https://doi.org/10.1021/acs.chemmater.3c01293
Chem. Mater. 2023, 35, 7020−7031

tected Silver Nanoclusters and Their Responsive Optical Properties. *Nat. Commun.* **2019**, *10*, 4032.
(47) Chevrier, D. M.; Conn, B. E.; Li, B.; Jiang, D. E.; Bigioni, T. P.; Chatt, A.; Zhang, P. Interactions between Ultrastable $Na_4Ag_{44}(SR)_{30}$ Nanoclusters and Coordinating Solvents: Uncovering the Atomic-Scale Mechanism. *ACS Nano* **2020**, *14*, 8433−8441.
(48) Hou, Y.; Wang, Y.; Xu, T.; Wang, Z.; Tian, W.; Sun, D.; Yu, X.; Xing, P.; Shen, J.; Xin, X.; Hao, J. Synergistic Multiple Bonds Induced Dynamic Self-Assembly of Silver Nanoclusters into Lamellar Frameworks with Tailored Luminescence. *Chem. Mater.* **2022**, *34*, 8013−8021.
(49) Wang, Z.; Zhu, Y. J.; Li, Y. Z.; Zhuang, G. L.; Song, K. P.; Gao, Z. Y.; Dou, J. M.; Kurmoo, M.; Tung, C. H.; Sun, D. Nuclearity Enlargement from $[PW_9O_{34}@Ag_{51}]$ to $[(PW_9O_{34})_2@Ag_{72}]$ and 2D and 3D Network Formation Driven by Bipyridines. *Nat. Commun.* **2022**, *13*, 1802.
(50) Li, B.; Huang, R. W.; Qin, J. H.; Zang, S. Q.; Gao, G. G.; Hou, H. W.; Mak, T. C. W. Thermochromic Luminescent Nest-Like Silver Thiolate Cluster. *Chem. −Eur. J.* **2014**, *20*, 12416−12420.
(51) Sun, Q.-Q.; Li, Q.; Li, H.-Y.; Zhang, M.-M.; Sun, M.-E.; Li, S.; Quan, Z.; Zang, S.-Q. Thermochromism and Piezochromism of an Atomically Precise High-Nuclearity Silver Sulfide Nanocluster. *Chem. Commun.* **2021**, *57*, 2372−2375.
(52) Zhang, S. S.; Alkan, F.; Su, H. F.; Aikens, C. M.; Tung, C. H.; Sun, D. An Atomically Precise Silver Nanocluster Co-Protected by Inorganic and Organic Ligands. *J. Am. Chem. Soc.* **2019**, *141*, 4460−4467.
(53) Su, Y. M.; Cao, Z. Z.; Feng, L.; Xue, Q. W.; Tung, C. H.; Gao, Z. Y.; Sun, D. Thermally Hypsochromic or Bathochromic Emissions? The Silver Nuclei Does Matter. *Small* **2022**, *18*, No. 2104524.
(54) Bootharaju, M. S.; Burlakov, V. M.; Besong, T. M. D.; Joshi, C. P.; Abdulhalim, L. G.; Black, D. M.; Whetten, R. L.; Goriely, A.; Bakr, O. M. Reversible Size Control of Silver Nanoclusters via Ligand-Exchange. *Chem. Mater.* **2015**, *27*, 4289−4297.
(55) Wei, X.; Chu, K.; Adsetts, J. R.; Li, H.; Kang, X.; Ding, Z.; Zhu, M. Nanocluster Transformation Induced by SbF_6^- Anions toward Boosting Photochemical Activities. *J. Am. Chem. Soc.* **2022**, *144*, 20421−20433.
(56) Dar, W. A.; Jana, A.; Sugi, K. S.; Paramasivam, G.; Bodiuzzaman, M.; Khatun, E.; Som, A.; Mahendranath, A.; Chakraborty, A.; Pradeep, T. Molecular Engineering of Atomically Precise Silver Clusters into 2D and 3D Framework Solids. *Chem. Mater.* **2022**, *34*, 4703−4711.
(57) Stamplecoskie, K. G.; Scaiano, J. C. Light Emitting Diode Irradiation Can Control the Morphology and Optical Properties of Silver Nanoparticles. *J. Am. Chem. Soc.* **2010**, *132*, 1825−1827.
(58) Callegari, A.; Tonti, D.; Chergui, M. Photochemically Grown Silver Nanoparticles with Wavelength-Controlled Size and Shape. *Nano Lett.* **2003**, *3*, 1565−1568.
(59) Lu, D.; Liu, Q.; Zhang, T.; Cai, Y.; Yin, Y.; Jiang, G. Stable Silver Isotope Fractionation in the Natural Transformation Process of Silver Nanoparticles. *Nat. Nanotechnol.* **2016**, *11*, 682−686.
(60) Raza, S.; Kadkhodazadeh, S.; Christensen, T.; Di Vece, M.; Wubs, M.; Mortensen, N. A.; Stenger, N. Multipole Plasmons and Their Disappearance in Few-Nanometre Silver Nanoparticles. *Nat. Commun.* **2015**, *6*, 8788.
(61) Stamplecoskie, K. G.; Pacioni, N. L.; Larson, D.; Scaiano, J. C. Plasmon-Mediated Photopolymerization Maps Plasmon Fields for Silver Nanoparticles. *J. Am. Chem. Soc.* **2011**, *133*, 9160−9163.
(62) Stefancu, A.; Gargiulo, J.; Laufersky, G.; Auguié, B.; Chiş, V.; Le Ru, E. C.; Liu, M.; Leopold, N.; Cortés, E. Interface-Dependent Selectivity in Plasmon-Driven Chemical Reactions. *ACS Nano* **2023**, *17*, 3119−3127.
(63) Naoi, K.; Ohko, Y.; Tatsuma, T. TiO_2 Films Loaded with Silver Nanoparticles: Control of Multicolor Photochromic Behavior. *J. Am. Chem. Soc.* **2004**, *126*, 3664−3668.
(64) Li, W.; Guo, Y.; Zhang, P. SERS-Active Silver Nanoparticles Prepared by a Simple and Green Method. *J. Phys. Chem. C* **2010**, *114*, 6413−6417.
(65) Tang, L.; Kang, X.; Wang, S.; Zhu, M. Light-Induced Size-Growth of Atomically Precise Nanoclusters. *Langmuir* **2019**, *35*, 12350−12355.
(66) Jana, A.; Jash, M.; Poonia, A. K.; Paramasivam, G.; Islam, M. R.; Chakraborty, P.; Antharjanam, S.; Machacek, J.; Ghosh, S.; Adarsh, K. N. V. D.; Base, T.; Pradeep, T. Light-Activated Intercluster Conversion of an Atomically Precise Silver Nanocluster. *ACS Nano* **2021**, *15*, 15781−15793.
(67) Walter, M.; Akola, J.; Lopez-Acevedo, O.; Jadzinsky, P. D.; Calero, G.; Ackerson, C. J.; Whetten, R. L.; Grönbeck, H.; Häkkinen, H. A Unified View of Ligand-Protected Gold Clusters as Superatom Complexes. *Proc. Natl. Acad. Sci. U. S. A.* **2008**, *105*, 9157−9162.
(68) Weerawardene, K. L. D. M.; Häkkinen, H.; Aikens, C. M. Connections between Theory and Experiment for Gold and Silver Nanoclusters. *Annu. Rev. Phys. Chem.* **2018**, *69*, 205−229.
(69) Liang, T.; Ren, L. U. Some Studies Concerning Rotating Axes and Polyatomic Molecules. *Phys. Rev.* **1935**, *47*, 552.
(70) Zhou, H.; Park, J. H.; Fan, F. R. F.; Bard, A. J. Observation of Single Metal Nanoparticle Collisions by Open Circuit (Mixed) Potential Changes at an Ultramicroelectrode. *J. Am. Chem. Soc.* **2012**, *134*, 13212−13215.
(71) Xiao, Y.; Fan, F. R. F.; Zhou, J.; Bard, A. J. Current Transients in Single Nanoparticle Collision Events. *J. Am. Chem. Soc.* **2008**, *130*, 16669−16677.
(72) Xiao, X.; Bard, A. J. Observing Single Nanoparticle Collisions at an Ultramicroelectrode by Electrocatalytic Amplification. *J. Am. Chem. Soc.* **2007**, *129*, 9610−9612.
(73) Zhou, H.; Fan, F. R. F.; Bard, A. J. Observation of Discrete Au Nanoparticle Collisions by Electrocatalytic Amplification Using Pt Ultramicroelectrode Surface Modification. *J. Phys. Chem. Lett.* **2010**, *1*, 2671−2674.
(74) Al-Zubeidi, A.; Ostovar, B.; Carlin, C. C.; Li, B. C.; Lee, S. A.; Chiang, W.-Y.; Gross, N.; Dutta, S.; Misiura, A.; Searles, E. K.; Chakraborty, A.; Roberts, S. T.; Dionne, J. A.; Rossky, P. J.; Landes, C. F.; Link, S. Mechanism for Plasmon-Generated Solvated Electrons. *Proc. Natl. Acad. Sci. U. S. A.* **2023**, *120*, No. e2217035120.
(75) Nakanishi, H.; Bishop, K. J. M.; Kowalczyk, B.; Nitzan, A.; Weiss, E. A.; Tretiakov, K. V.; Apodaca, M. M.; Klajn, R.; Stoddart, J. F.; Grzybowski, B. A. Photoconductance and Inverse Photoconductance in Films of Functionalized Metal Nanoparticles. *Nature* **2009**, *460*, 371−375.
(76) Bernardi, M.; Mustafa, J.; Neaton, J. B.; Louie, S. G. Theory and Computation of Hot Carriers Generated by Surface Plasmon Polaritons in Noble Metals. *Nat. Commun.* **2015**, *6*, 7044.
(77) Higaki, T.; Liu, C.; Zhou, M.; Luo, T. Y.; Rosi, N. L.; Jin, R. Tailoring the Structure of 58-Electron Gold Nanoclusters: $Au_{103}S_2(S\text{-}Nap)_{41}$ and Its Implications. *J. Am. Chem. Soc.* **2017**, *139*, 9994−10001.
(78) Zhou, M.; Jin, R.; Sfeir, M. Y.; Chen, Y.; Song, Y.; Jin, R. Electron Localization in Rod-Shaped Triicosahedral Gold Nanocluster. *Proc. Natl. Acad. Sci. U. S. A.* **2017**, *114*, E4697−E4705.
(79) Li, Q.; Zhou, M.; So, W. Y.; Huang, J.; Li, M.; Kauffman, D. R.; Cotlet, M.; Higaki, T.; Peteanu, L. A.; Shao, Z.; Jin, R. A Mono-Cuboctahedral Series of Gold Nanoclusters: Photoluminescence Origin, Large Enhancement, Wide Tunability, and Structure-Property Correlation. *J. Am. Chem. Soc.* **2019**, *141*, 5314−5325.

https://doi.org/10.1021/acs.chemmater.3c01293
Chem. Mater. 2023, 35, 7020−7031